International Communications in Heat and Mass Transfer 167 (2025) 109289

Contents lists available at ScienceDirect

International Communications in Heat and Mass Transfer

journal homepage: www.elsevier.com/locate/ichmt

Analysis of three-dimensional thermocapillary flows during PCM melting in large aspect ratio containers in microgravity using POD

P. Salgado Sánchez [a,*], X. Ruiz [b], J. Massons [b], J. Porter [a], J.M. Ezquerro [a], Jna. Gavaldà [b]

[a] E-USOC, Center for Computational Simulation, E. T. S. de Ingeniería Aeronáutica y del Espacio, Universidad Politécnica de Madrid, Madrid, Spain
[b] Facultat de Química, Universitat Rovira i Virgili, Tarragona, Spain

ARTICLE INFO

Keywords:
Phase change materials
Thermocapillary effect
Melting
Microgravity
POD

ABSTRACT

The three-dimensional thermocapillary-driven melting of a phase change material (PCM) in a large-aspect-ratio cuboidal domain in microgravity is investigated numerically. The dynamics within the liquid phase is characterized by various mode transitions that can affect the heat transfer rate. Here we describe the types of melting dynamics that can occur with a selection of three different applied temperature differences ΔT and four different choices of container width W. A proper orthogonal decomposition (POD) method using Singular Value Decomposition (SVD) is applied to determine the dominant modes that describe the melting process, with particular attention to the transition to oscillatory flow. It is found that the oscillatory dynamics are typically associated with an interaction between oblique and longitudinal hydrothermal traveling waves, and that the latter have a slightly lower frequency. The leading-order oscillatory modes may be symmetric with respect to the lateral midplane or not, depending on the applied temperature and the spanwise aspect ratio. Mode (frequency) splitting is sometimes observed, as well as secondary harmonic modes satisfying a 1:2 spatio-temporal resonance condition. These results show that PCM melting is a complex dynamical process involving competition among various hydrothermal traveling waves with distinct orientation and that symmetry-breaking and spatiotemporal resonance play prominent roles in the mode selection problem.

1. Introduction

Phase Change Materials (PCMs) are widely used for temperature control and to improve performance in a variety of heat-generating devices [1–5]. Their appeal relies on the fact that many materials absorb or release significantly more energy in changing their state of matter at the phase-transition temperature than they do in changing their temperature (by one degree, for example) when the phase is uniform. By selecting a material with a critical temperature within the desired range, the latent heat of the PCM increases the total thermal inertia of the configuration and reduces the magnitude of unwanted thermal variations.

Most common PCMs make use of the phase change between liquid and solid and fall into two main classes: organic and inorganic [6]. Organic PCMs, which are composed of hydrocarbons, are generally safer and more chemically stable than inorganic PCMs, which are normally based on salt hydrates (less commonly, metals). However, although organic PCMs also have the advantage of a high latent heat capacity, they suffer from low thermal conductivity compared to inorganic PCMs. This problem limits the rate at which they can absorb and release energy, making them less useful for systems that experience rapid changes in heat flux and temperature.

Since organic PCMs do not conduct heat well, their performance (in terms of responsiveness) can be improved by providing alternative pathways for heat flow via the incorporation of more conductive materials [7], the use of active heat transfer circuits [8,9], the addition of nanoparticles [10–12], or simply by encouraging convection within the liquid phase. Convective flow, when directed in the correct sense, can dramatically increase the heat transfer rate in the liquid and improve the ability of the PCM to absorb and store energy as latent heat [13–17]. In ordinary applications on ground, some amount of convection occurs naturally due to gravity and the temperature-dependent density of the material, which generates a buoyancy force. When heating from the side, for example, the buoyancy force tends to generate vortical flow drawing warm liquid upward, then across to the solid/liquid front, which accelerates melting. When heating from above, on the other hand, the buoyancy force opposes the downward movement of warm liquid to the melting front and can be detrimental to performance [18].

An interesting area of applications for PCMs is in space exploration [19], where temperature variations are a critical concern for

* Corresponding author.
E-mail address: pablo.salgado@upm.es (P. Salgado Sánchez).

https://doi.org/10.1016/j.icheatmasstransfer.2025.109289

Available online 8 July 2025

electrical and life-support systems, as well as fuel management [20–23]. In reduced gravity environments, natural convection can no longer be used to improve the performance of organic PCMs. However, if the PCM device is designed with a free surface, then thermal Marangoni convection provides an alternative mechanism for generating convective flow in the liquid phase; see [24–29] and references therein. This mechanism relies on the temperature dependence of surface tension, which leads to tangential stress at the free surface that drives convective motion. Most relevant PCM designs have solid boundaries on the hot and cold sides with the free surface transverse to those and aligned with the principal temperature gradient. Consequently, the associated Marangoni convection (unlike natural convection) always acts in the correct sense and transfers warm liquid, in regions of lower surface tension, to the cool boundary or melting front, where surface tension is higher.

The melting of a PCM under the influence of convective flow is a complex time-dependent process. The volume of the liquid phase increases over time while the location and shape of the melting front change. Both the average magnitude and the spatial distribution of the thermal gradients vary. The nature of the convective flow evolves throughout the melting process as well, often transitioning between distinct quasi-steady flow patterns, such as steady return flow and multicellular structures [30,31], and among different types of oscillatory dynamics, including oscillatory standing waves and hydrothermal traveling waves [32–38]. All of these changes affect the heat transfer rate and must be understood if reliable Marangoni-enhanced PCM devices are to achieve their full potential, particularly in space applications.

The "Effect of Marangoni Convection on Heat Transfer in Phase Change Materials" (MarPCM) project [39,40], which will be performed on the International Space Station (ISS) in 2026 (or later), will experimentally test the performance of Marangoni-enhanced PCMs in microgravity. A series of experiments will record the melting of PCMs in cuboidal [41] and cylindrical (melting bridge) [42] configurations and compare the cases with Marangoni convection to a reference cell with purely conductive heat transfer [24,43]. Previous numerical investigations are essential to predict and interpret the MarPCM experimental results, and a series of studies have considered the dynamics of PCM melting in both configurations, including dependence on the applied temperature difference, geometry (aspect ratio), boundary conditions, gravity level (if present), residual accelerations (g-jitter), and the addition of nanoparticles. The sequence of observed instabilities (bifurcations) has been described in terms of an effective time-dependent Marangoni number and aspect ratio [36].

Due to the number of relevant parameters and the need for numerous simulations, most of the work on Marangoni-driven PCM melting relies on two-dimensional (2D) approximations, ignoring lateral variations in cuboidal domains and azimuthal variations in cylindrical ones. It is crucial to compare these 2D predictions with (more costly) three-dimensional (3D) simulations to verify that the basic conclusions are correct and to understand the situations in which 3D effects can play an important role. This type of comparison was made by Seta et al. [44] who found that in cuboidal containers the average melting rate was quite similar to that of the 2D case (typically within 5% or less) as was the evolution of the solid/liquid front, particularly in the central plane. However, the onset of oscillatory dynamics tends to occur earlier in the full 3D case, and transverse modes can produce undulations in the shape of the melting front. Sometimes these transverse modes are reflection-symmetric (about the lateral midplane), and sometimes they are not.

The current paper builds on this work [44] and considers the influence of the lateral width on the dynamics of a melting PCM in a cuboidal container. Transverse dynamics are analyzed with special attention to the oscillatory regime. The modes describing melting dynamics are obtained using the Proper Orthogonal Decomposition (POD) method that, in this case, applies Singular Value Decomposition (SVD) to a matrix formed by a set of snapshots (images) representing the complete melting process. The SVD technique [45], which generalizes the usual eigenmode decomposition of a square matrix, is a robust and efficient method for generating a set of ordered orthogonal modes that best approximate the full melting process. Applications of SVD are widespread in many areas of science and engineering, including statistics [46], control [47], image processing [48–50] and reduced order models in fluid mechanics [51]. In the melting PCM system considered here, they are an accurate and convenient way to capture the important dynamics of the process and describe transitions. Furthermore, while they are obviously not Fourier modes, they tend to display a similar regularity of features such as relatively consistent wavenumbers and frequency content, which makes them relatively easy to interpret physically.

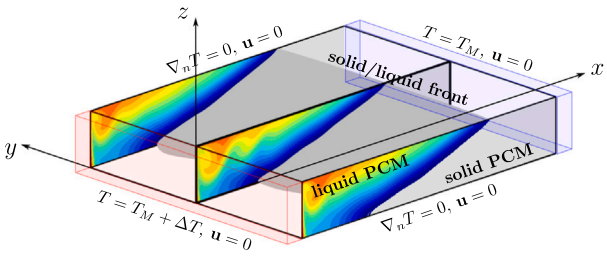

Fig. 1. Sketch of the 3D numerical model.

The paper is organized as follows. The setup, numerical scheme, and POD-based processing method used for the 3D simulations are summarized in Section 2. The main results are presented in Section 3, including the spatial structure of the dominant modes and spectrograms for the ones corresponding to oscillatory flow. Four different PCM widths and three different thermal forcing amplitudes are considered. Conclusions are given in Section 4.

2. Methodology

We consider a PCM confined in a cuboidal container with length $L = 22.5\,\text{mm}$ and height $H = 1.875\,\text{mm}$, which corresponds to a streamwise aspect ratio $\Gamma_H = L/H = 12$, and various widths of $W = 25$, 18.75, 12.5, 6.25 mm, which correspond, respectively, to the spanwise aspect ratios $\Gamma_W = L/W = 0.9, 1.2, 1.8$ and 3.6. The PCM undergoes a controlled phase transition from solid to liquid in microgravity driven by constant temperatures $T_M + \Delta T$ and T_M applied to the opposing walls at $x = 0, L$, respectively. The upper boundary of the PCM at $z = H$ is exposed to a layer of air. When melting begins, part of the PCM along this boundary is liquefied, and the temperature gradient along the liquid/air interface generates a corresponding gradient in surface tension that drives thermocapillary flow in the liquid phase. This convective flow both augments heat transfer and modifies the dynamics of the melting process. A sketch of the setup for the numerical model is shown in Fig. 1.

The properties of the PCM are assumed to be those of n-octadecane because reliable measurements of its thermophysical properties are available [10,52,53] and it has been selected for recent experiments in microgravity [24,25,43]. Table 1 lists the parameters used when numerically resolving the dynamics of the phase change with the enthalpy-porosity formulation of the Navier–Stokes equations. This formulation treats the solid/liquid interface using a continuous field f_l that varies smoothly between 0 (pure solid) and 1 (pure liquid) and eliminates the need to explicitly track the interface itself. A brief summary of the mathematical formulation and numerical simulations is provided below, with more details available in Refs. [54–57].

Table 1
Physical properties of n-octadecane, reproduced from [10,52,53]).

Melting temperature, T_M	28 °C
Liquid density, ρ_l	780 kg/m^3
Solid density, ρ_s	865 kg/m^3
Specific latent heat, L_f	243.5 kJ/kg
Liquid specific heat capacity, c_{pl}	2196 J/(kg K)
Solid specific heat capacity, c_{ps}	1934 J/(kg K)
Liquid conductivity, k_l	0.148 W/(m K)
Solid conductivity, k_s	0.358 W/(m K)
Dynamic viscosity, μ	3.541 mPa s
Surface tension at T_m, σ_0	27.54 mN/m
Thermocapillary coefficient, γ	8.44×10^{-5} N/(m K)

2.1. Numerical simulations

The flow within the liquid is assumed to be laminar and incompressible and, except for surface tension, all thermophysical properties are taken to be constant over the range of temperatures considered. The momentum and continuity equations are

$$\frac{\partial \mathbf{u}}{\partial t} + (\mathbf{u}\cdot\nabla)\mathbf{u} = -\frac{\nabla p}{\rho_l} + \nu\nabla^2\mathbf{u} + \frac{1}{\rho_l}\mathrm{DS}, \tag{1}$$

$$\nabla\cdot\mathbf{u} = 0, \tag{2}$$

where $\mathbf{u} = (u, v, w)$ is the velocity field in the Cartesian reference frame of Fig. 1, p is the pressure, ρ_l is the liquid density at a reference temperature, $\nu = \mu_l/\rho_l$ is the kinematic viscosity and DS is the Darcy source term [defined below in Eq. (6)].

The conservation of energy reads

$$\rho_l c_p\left(\frac{\partial T}{\partial t} + \mathbf{u}\cdot\nabla T\right) = \nabla\cdot(k\nabla T) - \mathrm{ES}, \tag{3}$$

where T is the temperature, c_p and k are the interpolated specific heat and thermal conductivity [see Eq. (5) below], and ES is a source term related to the phase change [defined below in Eq. (7)].

An essential part of the enthalpy-porosity formulation is the definition of the local liquid fraction field f_l that depends on T and varies between 0 (solid) and 1 (liquid). A linear interpolation is used to model f_l in 'mushy regions' where both solid and liquid phases coexist:

$$f_l = \begin{cases} 0 & T \le T_s, \\ 1 & T \ge T_M, \\ \frac{T-T_s}{T_M-T_s} & T_s < T < T_M. \end{cases} \tag{4}$$

Here, T_M and T_s are the liquidus and solidus temperatures, and we take $T_M - T_s = \Delta T_s = 1$ K to be the temperature interval defining the mushy region [25,26]. For n-octadecane, the values of ΔT_s reported in the literature (see, e.g., [58] and references therein) range from 1 K to 4 K.

The liquid fraction f_l is then used to define a linear interpolation of physical properties between the limiting solid and liquid values:

$$(c_p, k) = (c_{ps}, k_s)(1 - f_l) + (c_{pl}, k_l) f_l. \tag{5}$$

The liquid fraction also couples the conservation of momentum and energy via the (vector) Darcy source term, DS, which takes the form of a Carman–Kozeny equation,

$$\mathrm{DS} = \frac{C(1-f_l)^2}{\delta + f_l^3}\mathbf{u}, \tag{6}$$

and is used to smoothly reduce the velocity field from $\mathbf{u}$ in the liquid to 0 in the solid. The permeability (or Darcy) coefficient C controls the strength of this source term while δ is a small constant that prevents division by 0. Note that if the PCM is completely liquefied ($f_l = 1$ everywhere), then DS vanishes and the usual Navier–Stokes equations hold. If, on the other hand, the PCM is completely solid ($f_s = 0$ everywhere), then DS becomes $\mathcal{O}(C/\delta) \gg 1$ and $\mathbf{u}$ vanishes, as expected. In the mushy region, DS is finite and modifies the Navier–Stokes equations. The value of C, which reflects the morphology of the PCM, has a strong influence on the dynamics in this region and should be adjusted according to experimental results. Here we use $C = 1.6\times10^6$ kg m^3 s and $\delta = 10^{-3}$ to be consistent with previous work [42,59,60].

The source term ES in Eq. (3) is given by

$$\mathrm{ES} = \rho_l L_f\left(\frac{\partial f_l}{\partial t} + \mathbf{u}\cdot\nabla f_l\right), \tag{7}$$

and describes the conservation of energy in the form of latent heat L_f as the phase change proceeds. Note that the effect of the advective term $\mathbf{u}\cdot\nabla f_l$ can be neglected in sufficiently narrow mushy regions.

The set of governing Eqs. (1)–(7) is closed with appropriate boundary conditions for $\mathbf{u}$ and T:

- No-slip and isothermal boundaries at $x = 0, L$:

$$\mathbf{u} = 0, \quad T = T_M + \Delta T, T_M. \tag{8}$$

  Here, we take $\Delta T = 20, 30, 40$ K.
- No-slip and adiabatic boundaries at $y = \pm W/2$ and $z = 0$:

$$\mathbf{u} = 0, \quad k\nabla T\cdot\mathbf{n} = 0, \tag{9}$$

  where $\mathbf{n}$ is a unit vector normal to the boundary.

The use of adiabatic conditions on the lower and lateral walls makes it easy to compare with previous 2D [25,26,35,36] and 3D simulations [44]. Note that there is no assumption of symmetry. Although this could be done to reduce the computational domain and make the simulations less expensive, it would prevent the observation of asymmetric solutions.

The free surface at $z = H$ is assumed to be adiabatic and perfectly flat. This geometric simplification is consistent with the design of the MarPCM experiment, where the contact line will be pinned to a sharp edge of the container [40], and with the small capillary number $\mathrm{Ca} = (\gamma\Delta T)/\sigma_0 \le 0.123$, which suggests small surface deformation [35,61]. The fixed surface also means that the change in volume between the solid and liquid phases is neglected; simulations with the same assumption were validated against experiments in Ref. [39].

At the free surface, the viscous and thermocapillary forces are equal:

$$\mu\nabla\mathbf{u}\cdot\mathbf{e}_z = \gamma\nabla T\cdot(\mathbf{e}_x, \mathbf{e}_y, 0), \tag{10}$$

where $(\mathbf{e}_x, \mathbf{e}_y, \mathbf{e}_z)$ are unit vectors in the Cartesian coordinate system; see Fig. 1.

The system is solved with the finite-volume method implemented in the OpenFOAM package. Discretization is second-order in space and time. Since the PCM is initially solid, the velocity field at $t = 0$ is null and the temperature T_0 is uniform and below the solidus temperature T_s. The time step, initially set at 0.001 s is limited when necessary by the maximum Courant–Friedrich–Levy condition with the restrictive value of 0.25. The momentum and continuity equations are solved using the PIMPLE algorithm, with the temperature field calculated at each PIMPLE iteration using a linearization of the discretized source term [57,62–64]. The final linear system of equations is solved using the Geometric-Algebraic Multi-Grid (GAMG) method. The tolerance is set to 10^{-8} for pressure, velocity, and temperature fields and a diagonal incomplete-LU (asymmetric DILU) preconditioner is used for the matrices. To reduce computation time, the cuboidal domain is divided into eight or twelve smaller volumes with the Scotch domain decomposition method [65] and solved in parallel.

Validation of the code is described elsewhere [42,60]. Elementary parallelepipedic cells of volume $0.225\times0.625\times0.054$ mm^3 are selected, with the longer dimension (0.625 mm) along the y-axis where the temperature gradients are weaker and less resolution is required. The number of mesh nodes is therefore $N = n_x\times n_y\times n_z = 100\times W/(0.625)\times35$.

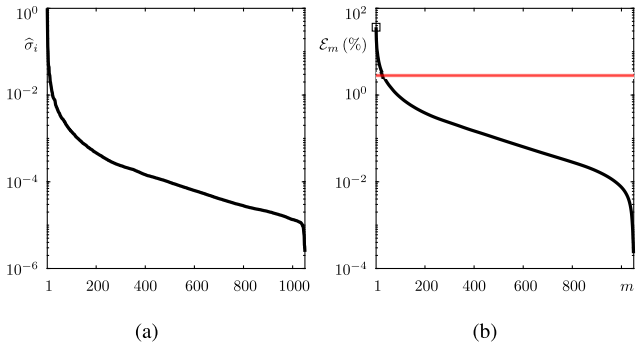

Fig. 2. Example of SVD for the melting process with $\Delta T = 20\,\mathrm{K}$ and $W = 25\,\mathrm{mm}$: (a) normalized singular values $\hat{\sigma}_m$ and (b) relative error $\mathcal{E}_m$ (in %) of the approximation with m modes.

2.2. POD and principal mode analysis

The POD method is used to process the results of the simulations. First, the velocity and temperature fields are rescaled with

$$(\mathbf{u},\, T) \rightarrow (u_c\,\hat{\mathbf{u}},\, T_M + \Theta\,\Delta T), \tag{11}$$

where $\hat{\mathbf{u}}$ and Θ are the dimensionless velocity and temperature fields and u_c is a characteristic velocity of the flow along the x-axis. These rescaled quantities are interpolated at n_t equispaced times up to the completion of melting. At each time step, the matrix (snapshot) containing the dimensionless fields $(\hat{\mathbf{u}},\, \Theta)$ at each mesh node is reshaped into a column vector. The snapshots are then stacked into a single matrix $\mathbf{A} \in \mathbb{R}^{4N \times n_t}$ containing information that describes the entire melting process, and this is done for each choice of ΔT and W.

Using the SVD method [45], the normalized matrix $\mathbf{A}$ is decomposed in the form:

$$\mathbf{A} = \mathbf{U}\,\boldsymbol{\sigma}\,\mathbf{V}^T, \tag{12}$$

where $\mathbf{U} \in \mathbb{R}^{4N \times 4N}$ and $\mathbf{V} \in \mathbb{R}^{n_t \times n_t}$ are, respectively, the left and right singular vectors, $\boldsymbol{\sigma} \in \mathbb{R}^{4N \times n_t}$ is a diagonal matrix containing the singular values of the decomposition in order of decreasing magnitude, and the superscript T denotes the transpose. Fig. 2(a) shows the normalized singular values $\hat{\sigma}_i$,

$$\hat{\sigma}_i = \frac{\sigma_i}{\sigma_1}, \tag{13}$$

for the case of $\Delta T = 20\,\mathrm{K}$ and $W = 25\,\mathrm{mm}$, where a rapid decrease is observed in $\hat{\sigma}_i$. This indicates that the largest singular values contain most of the relevant information of $\mathbf{A}$. The matrix $\mathbf{A}$ may thus be approximated by considering the first m singular values as

$$\mathbf{A}_m \approx \sum_{i=1}^{m} U_i\,\sigma_i\,V_i^T = \sum_{i=1}^{m} \hat{\mathbf{U}}_i, \tag{14}$$

where U_i, V_i and σ_i are the ith singular vectors and the associated singular value, respectively, and $\hat{\mathbf{U}}_i = U_i\,\sigma_i\,V_i^T$. Anticipate that $\hat{\mathbf{U}}_i$ is the (scaled) temporal evolution of the ith singular mode.

The residual of this low-rank approximation, measured using the Frobenius norm (see the Eckart–Young–Mirsky theorem [66,67]), is

$$\|\mathbf{A} - \mathbf{A}_m\|_F = \sqrt{\sum_{i=1}^{n_t} \sigma_i^2} - \sqrt{\sum_{i=1}^{m} \sigma_i^2} = \sqrt{\sum_{i=m+1}^{n_t} \sigma_i^2}, \tag{15}$$

and can be also expressed as a relative error $\mathcal{E}_m$ with respect to the norm of $\mathbf{A}$:

$$\mathcal{E}_m = \frac{\sqrt{\sum_{i=m+1}^{n_t} \sigma_i^2}}{\sqrt{\sum_{i=1}^{n_t} \sigma_i^2}}. \tag{16}$$

This relative error is shown in Fig. 2(b). Note that with relatively few modes, $\mathbf{A}_m$ approximates the full melting process with negligible error. In this work, we consider the first 32 modes of the SVD factorization, which results in a relative error of approximately 5% (marked with a red horizontal line in the figure) in all cases.

The left singular vectors arising from the SVD decomposition constitute a basis of orthonormal modes satisfying $U_i \cdot U_j^T = \delta_{ij}$, where δ_{ij} is the Kronecker delta. Furthermore, these modes may be interpreted physically, as discussed below. The right singular vectors provide normalized amplitudes associated with each U_i.

3. Results

The results of numerical simulations and subsequent POD-based processing are discussed in this section. Three applied temperature differences are considered: $\Delta T = 20, 30$ and $40\,\mathrm{K}$, along with four decreasing values of container width: $W = 25$, 18.75, 12.5 and 6.25 mm. These widths correspond to increasing values of the spanwise aspect ratio of $\Gamma_W = L/W = 0.9$, 1.2, 1.8 and 3.6, respectively.

3.1. $W = 25\,mm$ ($\Gamma_W = 0.9$)

We first describe the results for $\Delta T = 20\,\mathrm{K}$ and give a physical interpretation of the orthogonal modes (and amplitudes) obtained via SVD; see Section 2.2.

In panels (b–g) of Fig. 3, the first six modes of the SVD factorization are shown in terms of the dimensionless temperature field Θ. The first mode, U_1, represents a kind of weighted average of velocity and temperature throughout the melting process. U_1 can be thought of as the mode with the largest wavelength $\lambda_x \sim 2L$ along the streamwise direction, capturing the characteristic temperature variation throughout the entire process. The mode U_2 is reminiscent of the first harmonic in a Fourier series with a shorter wavelength $\lambda_x \sim L$. The modes $U_3 - U_6$ are roughly analogous to higher-order terms (of higher spatial wavenumber) in such a Fourier series.

As noted above, the ith right singular vector V_i represents the normalized amplitude associated with the corresponding mode U_i required to reconstruct $\mathbf{A}$. Fig. 3(a) shows the amplitudes V_i of the first six modes, scaled with the corresponding (normalized) singular value $\hat{\sigma}_i$; see Eq. (13). The colors of these curves coincide with those of the labels identifying the six modes in the right panels. One can see that the principal frequency at which these amplitudes vary in time increases with i along with the dominant spatial wavenumber, similar to what would be expected in a Fourier series. The time series for the mode amplitudes $\hat{\sigma}_i V_i$ in this figure also reveal the appearance of comparably small-amplitude high-frequency ($\sim 0.2\,\mathrm{Hz}$) oscillations beyond $t \approx 500\,\mathrm{s}$, which indicates the presence of oscillatory flow during the melting process. However, these first six modes should be thought of as quasi-steady in nature since they only overlap slightly with the oscillatory thermocapillary flow.

The SVD modes U_7 and U_8, on the other hand, are directly associated with the transition to oscillatory flow. Fig. 4 shows the normalized amplitudes V_i [panels (a, d)] and the associated spectrogram [panels (b, e)] for these modes, which reveal that the oscillatory flow is characterized by two main frequencies near 0.2 Hz. The higher of these has the larger amplitude and appears at $t \approx 400\,\mathrm{s}$ while the lower one emerges later at $t \approx 500\,\mathrm{s}$. The difference between these two frequencies is responsible for the slow modulation observed in V_i. In contrast to modes $U_1 - U_6$, the amplitude of the oscillations in modes U_7 and U_8 increases rapidly above onset and soon dominates over the slower behavior observed before.

The different modes obtained via SVD may be characterized, approximately, by different spatial wavenumbers (equivalently, wavelengths) estimated by counting the number of pairs of hot and cold spots in each direction. For the oscillatory modes U_7 and U_8, one finds, in the streamwise direction, that $\lambda_x \sim L/4$ and the associated

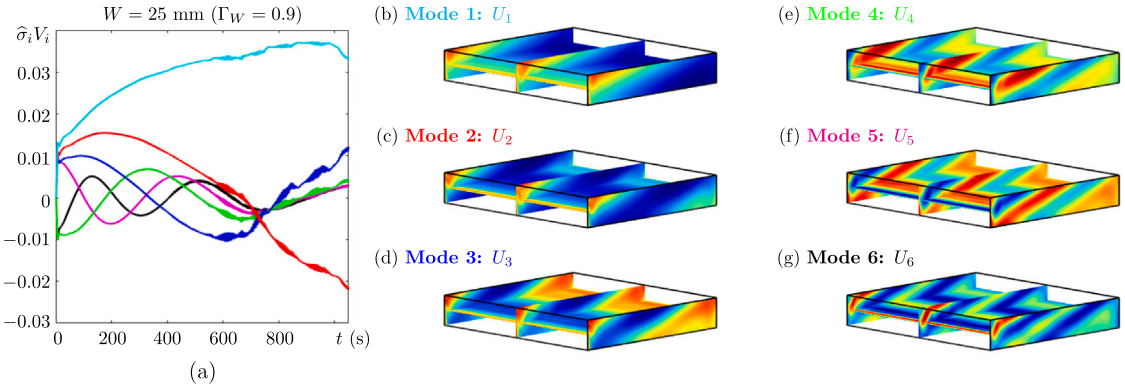

Fig. 3. Example of the first six SVD modes for $\Delta T = 20\,\mathrm{K}$ and $W = 25\,\mathrm{mm}$ ($\Gamma_W = 0.9$): (a) scaled amplitudes $\hat{\sigma}_i V_i$ and (b–g) singular vectors U_i.

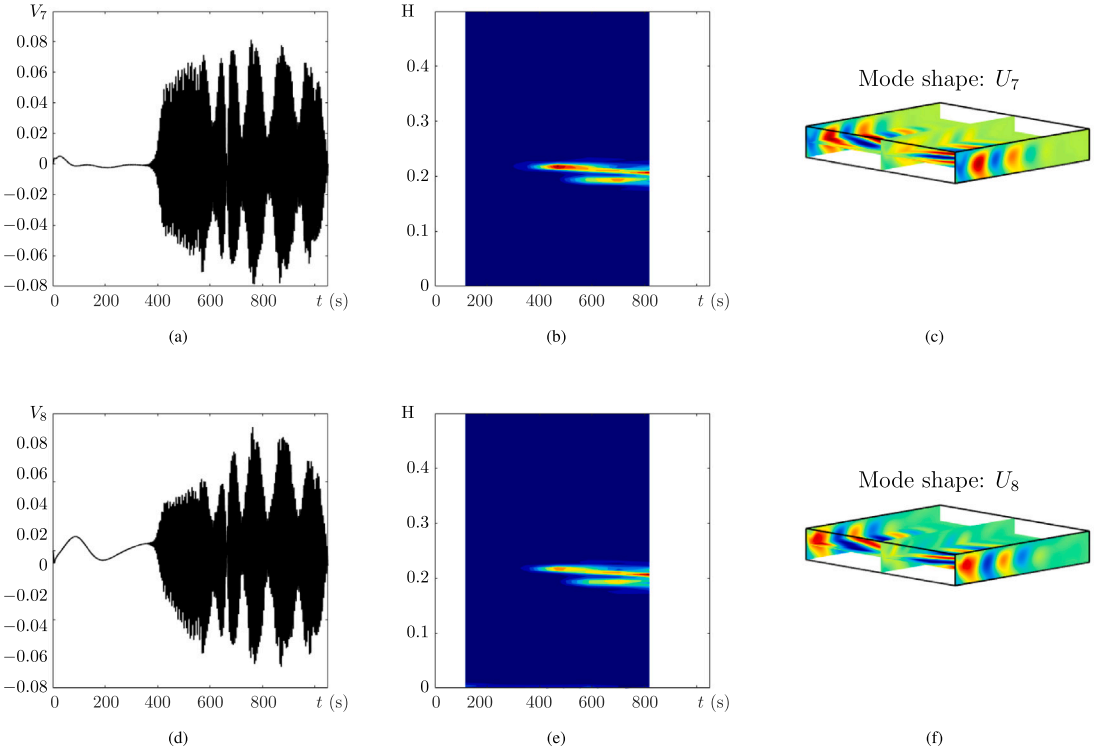

Fig. 4. Detailed view of (a–c) U_7 and (d–f) U_8 for $\Delta T = 20\,\mathrm{K}$ and $W = 25\,\mathrm{mm}$ ($\Gamma_W = 0.9$), showing their mode shapes (c, f), time series for their normalized amplitudes V_i (a, d) and the corresponding spectrograms (b, e). The approximation $\mathbf{A}_8$ and the HTW complete evolution $\hat{\mathbf{U}}_7 + \hat{\mathbf{U}}_8$ can be visualized in the supplementary video 'video_S2'.

dimensionless wavenumber is $\hat{k}_x = k_x L/(2\pi) \sim 4$. In the spanwise direction, $\lambda_y \sim W/2$ and the associated dimensionless wavenumber is $\hat{k}_y = k_y L/(2\pi) \sim 2\,\Gamma_W$. In the vertical direction, there is only one temperature spot, so $\lambda_z \sim 2H$ and $\hat{k}_z = k_z L/(2\pi) \sim 0.5\,\Gamma_H$. Recall that $\Gamma_H = 12$ throughout this analysis. This series of hot and cold spots, resembling stripes or rolls, is characteristic of a hydrothermal traveling wave (HTW) [26].

The role of different SVD modes in representing the melting dynamics can be understood better with the help of the supplementary video 'video_S1', which shows approximations of the melting process for $\mathbf{A}_m$ with $m = 1$, 2, 4, 8, 16 and 32.

Although the leading-order SVD modes can usually be given physical interpretations in analogy with Fourier modes, it should be remembered that they are derived from the features of the images (snapshots) of the full melting process without reference to frequency or wavenumber and are, consequently, more complicated than simple harmonic functions. They do not need to satisfy the boundary conditions individually — only in aggregate — and the 'wavenumbers' should be considered as rough estimates only. The representation of phase can be more complicated too. For example, an idealized system with a pure (one-dimensional, sinusoidal) traveling wave has a spatial Fourier decomposition consisting of two modes with time-dependent amplitudes: $\sin(kx \pm \omega t) = \cos(\omega t)\sin(kx) \pm \sin(\omega t)\cos(kx)$. The SVD decomposition similarly requires at least two modes to describe a traveling wave, and, for the PCM melting process studied here, the leading-order oscillatory modes tend to come in pairs, like U_7 and U_8 in Fig. 4, with singular values of similar magnitude, analogous spatial structure (but shifted in phase), and approximately the same spectrogram. However, higher-order SVD modes may be more complicated to interpret, with more than two modes sometimes associated with the same type of wave.

Another complication arises from the time dependence of the melting process and the changing liquid domain. This means that the relevance of a given SVD mode can vary significantly in time and higher-order modes, corresponding to smaller σ_i, may still be quite important for the physical interpretation of the melting process. For example, although the HTWs remain until (and beyond) the completion

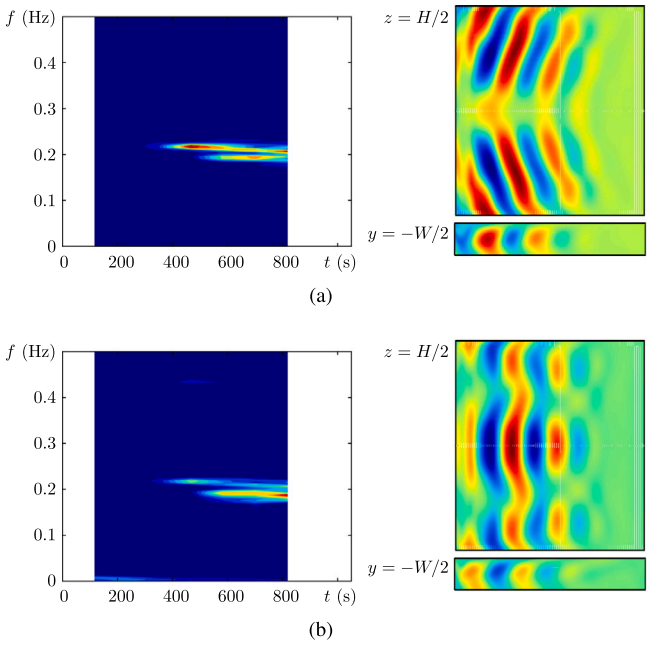

Fig. 5. Principal oscillatory modes for $W = 25\,\text{mm}$ ($\Gamma_W = 0.9$) and $\Delta T = 20\,\text{K}$: (a) U_7, (b) U_{11}. The temporal dynamics of these modes can be viewed in the supplementary videos 'video_S2' and 'video_S3', which show $\hat{\mathbf{U}}_7 + \hat{\mathbf{U}}_8$ and $\hat{\mathbf{U}}_{11} + \hat{\mathbf{U}}_{13}$, respectively.

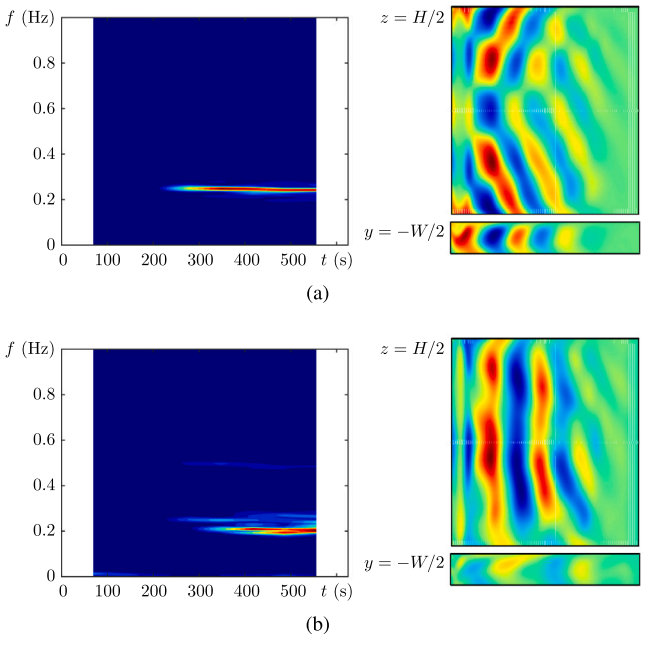

Fig. 6. Principal oscillatory modes for $W = 25\,\text{mm}$ ($\Gamma_W = 0.9$) and $\Delta T = 30\,\text{K}$: (a) U_6, (b) U_{11}.

of the phase change, the temperature field of U_7 and U_8 is concentrated in the first half of the domain, corresponding to an earlier period of melting. The explanation for this apparent contradiction is found in additional higher-order modes with a similar HTW structure that are biased toward the middle or second half of the domain. These modes have a smaller σ_i since they appear later and affect a smaller fraction of the melting process. A similar thing applies to any physical phenomenon that is relevant only during a particular (relatively short) phase of the melting; higher-order SVD modes will be needed to describe it. An example of this is provided later in Section 3.3.

Symmetry is an important property of the thermocapillary flow that depends critically on the lateral aspect ratio Γ_W and thermal forcing ΔT. In this case, the dominant SVD modes are all symmetric with respect to the lateral midplane of the container at $y = 0$, including the oscillatory modes U_7 and U_8. This reflection symmetry persists throughout the entire melting process.

Fig. 5 shows the spectral content and spatial structure, projected onto the planes $z = H/2$ and $y = -W/2$, of the two most dominant oscillatory modes with distinct features, for $\Delta T = 20\,\text{K}$. The strongest mode, shown in panel (a), is the same SVD mode U_7 discussed above (U_8 is its phase-shifted partner). It is characterized by $(\lambda_x, \lambda_y, \lambda_z) \sim (L/4, W/2, 2H)$ and dimensionless wavenumbers $(K_x, K_y, K_z) = (\hat{k}_x, \hat{k}_y\,\Gamma_W^{-1}, \hat{k}_z\,\Gamma_H^{-1}) \sim (4, 2, 0.5)$. Note that, since $K_z \sim 0.5$, the maximum amplitude occurs near $z = H/2$, which motivates the selection of this plane to illustrate the results. The spectrogram of U_7 exhibits two main frequencies at $f \simeq 0.185\,\text{Hz}$ and $f \simeq 0.219\,\text{Hz}$ with the higher one appearing first and having a higher average amplitude. As noted above, this mode is symmetric with respect to the lateral midplane.

Note that the low-dimensional approximation achieved by SVD offers a convenient way to separate different features of the melting process according to their quasi-steady or oscillatory nature, as well as other properties of interest. For instance, one can express Eq. (14) as

$$\mathbf{A}_m = \sum_{i=1}^{m} \hat{\mathbf{U}}_i = \sum_{\text{S}} \hat{\mathbf{U}}_i + \sum_{\text{1st}} \hat{\mathbf{U}}_i + \sum_{\text{2nd}} \hat{\mathbf{U}}_i + \cdots, \tag{17}$$

where the subscript 'S' refers to steady modes, and subscripts '1st', '2nd', etc., refer to oscillatory modes of distinct character. This separation could be used to analyze each HTW separately. The dynamics of the primary HTW mode, for example, is well captured by $\hat{\mathbf{U}}_7 + \hat{\mathbf{U}}_8$, and can be visualized in the supplementary video 'video_S2'. Such an approach is similar to subtracting the average temperature field over one oscillation cycle [36].

The next oscillatory mode with different qualitative features is U_{11} (its phase-shifted partner is U_{13}), which is shown in panel (b). This mode displays spatial variations with wavenumbers similar to U_7, but its dominant frequency is the lower one, at 0.185 Hz. The other important distinction between U_7 and U_{11} is in the spatial structure of the temperature field in a horizontal (xy) plane, as seen in the midplane $z = H/2$. The mode U_7 can be described as a series of stripes (rolls) with a wavevector making an angle of $\alpha \approx \pm\tan^{-1}(\lambda_x/\lambda_y) = \pm\tan^{-1}(2\Gamma_W/4) \simeq \pm 24°$ with respect to the negative x-axis. This angle gives the direction in which the HTWs travel within this melting PCM system and is consistent [33] with the large Prandtl number (52.5) of n-octadecane. The stripes in the temperature field of U_{11}, on the other hand, are (on average) associated with a wavevector oriented at 0° and thus with longitudinal motion. The temporal dynamics of this mode can be seen in supplementary video 'video_S3', which shows $\hat{\mathbf{U}}_{11} + \hat{\mathbf{U}}_{13}$. This mode is also symmetric with respect to the lateral midplane of the container.

The most important SVD modes representing oscillatory thermocapillary convection suggest that, in this case, there is an interaction between two types of HTWs, one traveling longitudinally, in the upstream direction (cold to hot), and one traveling obliquely at an angle of 24° with respect to this. The oblique HTW has a slightly higher dominant frequency than the longitudinal one. The interaction between both waves can be examined in the supplementary video 'video_S1' by comparing the approximation $\mathbf{A}_8$ (with the oblique but not the longitudinal mode) with $\mathbf{A}_{16}$ or $\mathbf{A}_{32}$ (which include the longitudinal HTW).

Fig. 6 shows the spectral content and spatial structure, projected onto the planes $z = H/2$ and $y = -W/2$, of the two dominant oscillatory modes with distinct features (U_6 and U_{11}) for $\Delta T = 30\,\text{K}$. The structures of these modes are broadly similar to those of the corresponding modes (U_7 and U_{11}) with $\Delta T = 20\,\text{K}$ and they display similar spatial variations with the same dominant wavenumbers.

Symmetry is one notable difference compared to the earlier case. The oscillatory flow for $\Delta T = 30\,\text{K}$ is clearly asymmetric with respect

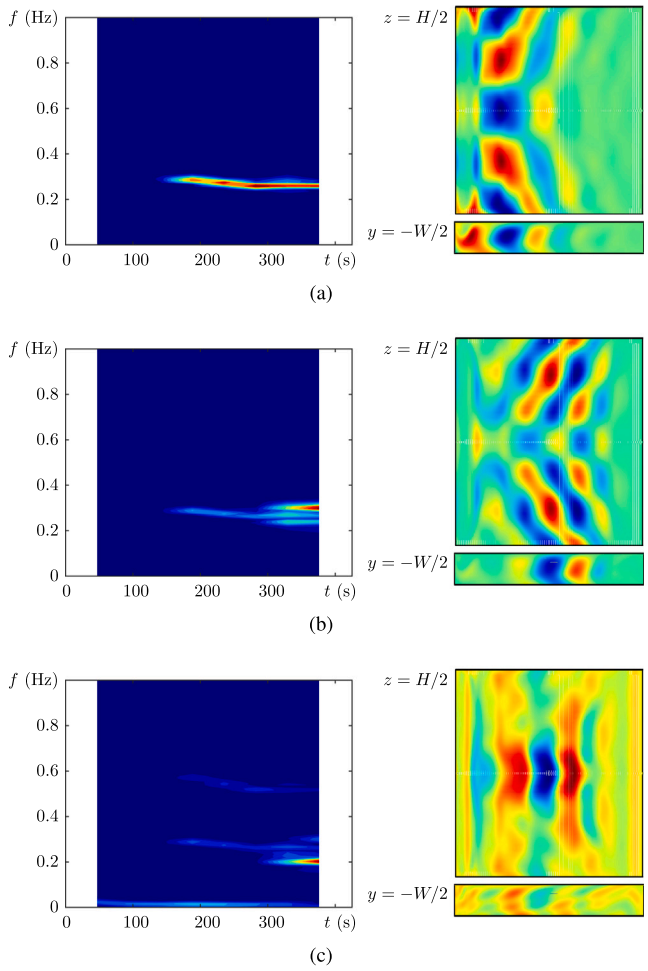

Fig. 7. Principal oscillatory modes for $W = 25\,\text{mm}$ ($\Gamma_W = 0.9$) and $\Delta T = 40\,\text{K}$: (a) U_6, (b) U_{12}, (c) U_{21}. The temporal dynamics of (a) can be seen in supplementary video 'video_S4', which shows $\widehat{\mathbf{U}}_6 + \widehat{\mathbf{U}}_8$.

to the reflection $y \to -y$. This asymmetry is greater within the part of the domain near the cold wall than near the hot wall. In fact, close to the cold wall, the HTW represented by mode U_6 (and U_8) travels primarily in the $-y$ direction (from $y = W/2$ to $y = -W/2$) at an angle of $\alpha \approx \tan^{-1}(2\Gamma_W/3.5) \simeq 27°$ with respect to the upstream ($-x$) direction. This angle is slightly more than for the oblique HTW with $\Delta T = 20\,\text{K}$. Note that, since the equations and initial conditions are symmetric, one can also find the mirror image of this solution, with HTWs that travel primarily in the $+y$ direction near the cold wall.

The second strongest (qualitatively distinct) oscillatory mode is U_{11} (its phase-shifted partner is U_{13}), which is again primarily associated with the longitudinal upstream HTW motion. It is also asymmetric. The spectrograms for the two modes indicate that, as before, the longitudinal mode has a lower frequency, with $f \simeq 0.203\,\text{Hz}$, than the oblique mode, with $f \simeq 0.246\,\text{Hz}$. These two frequencies are more separated than with $\Delta T = 20\,\text{K}$, as is the spectral content of each mode, a fact that suggests less interaction between the two types of HTWs.

Fig. 7 shows the results for the highest thermal forcing of $\Delta T = 40\,\text{K}$. The first appearance of oscillatory flow at $t \approx 150\,\text{s}$, when the melting front is close to two-thirds of the way to the cold boundary, is associated with the mode U_6 in panel (a). This mode (as well as its phase-shifted partner U_8) is characterized by the dimensionless wavenumbers $(K_x, K_y, K_z) \sim (3, 2, 0.5)$ and a dominant frequency $f = 0.261\,\text{Hz}$. As in the case of $\Delta T = 20\,\text{K}$ (but not $\Delta T = 30\,\text{K}$), this mode is symmetric under $y \to -y$. The temporal dynamics of this mode can be seen in supplementary video 'video_S4', which shows $\widehat{\mathbf{U}}_6 + \widehat{\mathbf{U}}_8$.

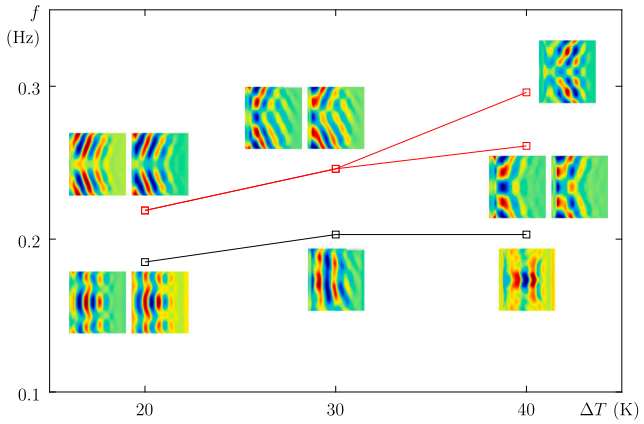

Fig. 8. Diagram summarizing the principal oscillatory modes for $W = 25\,\text{mm}$ ($\Gamma_W = 0.9$). The panel shows the dominant frequencies and spatial structures versus the applied thermal forcing ΔT.

As melting progresses and the liquid fraction increases, the first oscillatory mode loses strength while a second mode (represented by U_{12}) appears at $t \approx 300\,\text{s}$, when the upper, leading edge of the melting front has already reached the cold boundary. This mode transition is to another symmetric HTW with higher (dominant) wavenumbers in the x and y directions: $(K_x, K_y, K_z) \sim (4, 3, 0.5)$. The principal frequency of $f = 0.296\,\text{Hz}$ is also higher than for U_6. The spatial structure of the mode shows larger waves in the vicinity of the cold boundary (and/or the melting front) that decrease in amplitude as they approach the hot wall, consistent with previous results in 2D domains [35]. In this case, the modal decomposition of the HTW dynamics is more complicated than a single pair, with U_{12} accompanied by the modes U_{14}–U_{18}.

As in the two cases with lower thermal forcing, there is an approximately longitudinal mode, U_{21} (and its phase-shifted partner U_{22}), which emerges at $t \approx 300\,\text{s}$ along with U_{12}; it is shown in panel (c). The dominant frequency of this mode is $f = 0.203\,\text{Hz}$ and its spatial wavenumbers are $(K_x, K_y, K_z) \sim (3, 0.5, 0.5)$. Both of these features of the longitudinal HTW mode are largely insensitive to the increase in ΔT.

The principal oscillatory modes for $W = 25\,\text{mm}$ ($\Gamma_W = 0.9$) are summarized in Fig. 8, which indicates how the frequencies of the oblique and longitudinal HTWs change with ΔT and includes insets showing their spatial structure in the $z = H/2$ plane. The primary oblique HTW mode (red markers) shows a monotonic increase in frequency with ΔT and a frequency splitting between 30 K and 40 K, corresponding to a mode transition during the latter stage of melting. In contrast, the longitudinal HTW mode (black markers) is less sensitive to the thermal gradient, with a relatively small frequency increase between $\Delta T = 20\,\text{K}$ and 30 K and none at 40 K. The oscillatory flow is symmetric with respect to lateral reflection for $\Delta T = 20\,\text{K}$ and 40 K and asymmetric for $\Delta T = 30\,\text{K}$.

3.2. $W = 18.75\,mm$ ($\Gamma_W = 1.2$) and $W = 12.5\,mm$ ($\Gamma_W = 1.8$)

The same analysis in the case of $W = 18.75\,\text{mm}$, which corresponds to a spanwise aspect ratio of $\Gamma_W = 1.2$, produces the results summarized in Fig. 9(a). Again, the principal (qualitatively distinct) oscillatory modes are shown for three increasing values of ΔT in terms of their frequency and spatial structure in the planes $z = H/2$ and $y = -W/2$.

For $\Delta T = 20\,\text{K}$, the primary oscillatory mode (corresponding to U_7–U_9) is characterized by $(K_x, K_y, K_z) \sim (4, 1.5, 0.5)$ and is reflection symmetric with respect to the lateral midplane; these features are similar to those of the principal mode observed for $\Gamma_W = 0.9$ and the same thermal forcing. This mode exhibits two dominant frequencies at $f \simeq 0.199\,\text{Hz}$ and $f \simeq 0.234\,\text{Hz}$, which are slightly higher than for $\Gamma_W =$

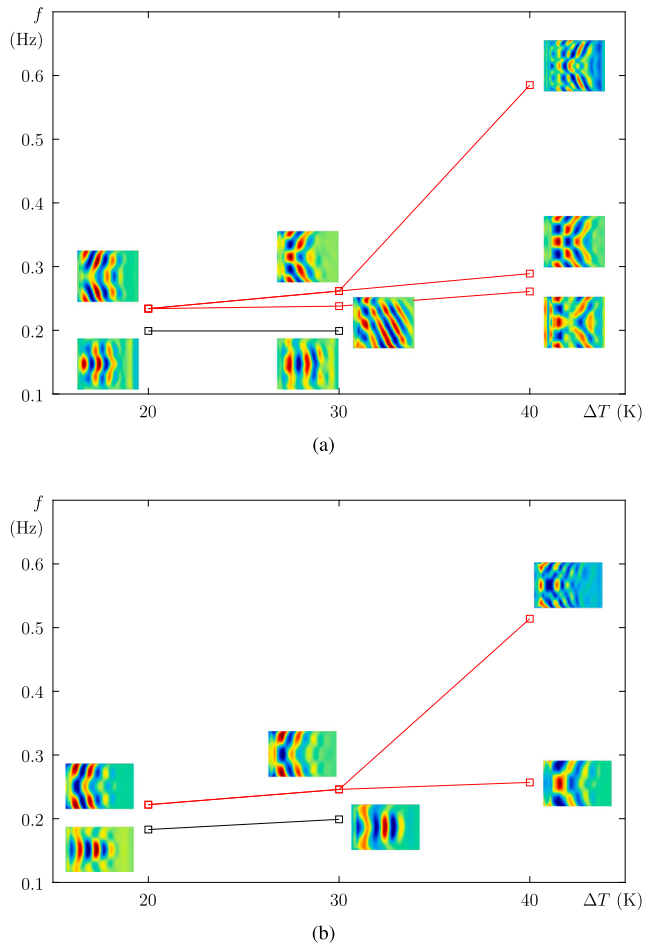

Fig. 9. Diagrams summarizing the principal oscillatory modes for (a) $W = 18.75\,\text{mm}$ ($\Gamma_W = 1.2$) and (b) $W = 12.5\,\text{mm}$ ($\Gamma_W = 1.8$). Each panel shows the dominant frequencies and spatial structures versus the applied thermal forcing ΔT.

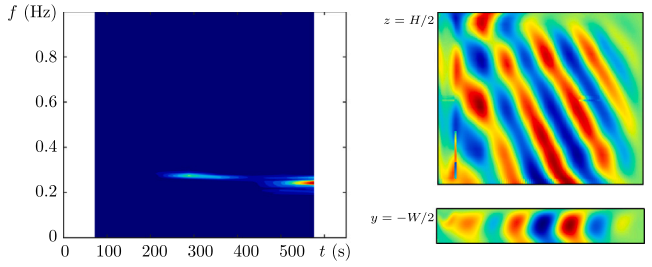

Fig. 10. First asymmetric mode for $W = 18.75\,\text{mm}$ ($\Gamma_W = 1.2$) and $\Delta T = 30\,\text{K}$. The temporal dynamics of this mode can be seen in supplementary video 'video_S5'.

0.9. Similarly, the second mode (corresponding to U_{13} and U_{16}–U_{18}) represents traveling waves that are on average moving longitudinally. This mode is characterized by $f \simeq 0.199\,\text{Hz}$.

For $\Delta T = 30\,\text{K}$, the primary oscillatory mode (corresponding to U_6 and U_8) is again characterized by $(K_x, K_y, K_z) \sim (4, 2, 0.5)$ and has a spatial structure that is approximately symmetric with respect to the lateral midplane. These features are shared with the principal oscillatory mode observed for $\Gamma_W = 0.9$ and the same thermal forcing. The associated spectrogram shows one dominant frequency at $f \simeq 0.262\,\text{Hz}$, which is slightly higher than for $\Gamma_W = 0.9$. The second strongest distinct oscillatory mode, which is characterized by the same wavenumbers but a slightly lower frequency of $f \simeq 0.238\,\text{Hz}$, is shown by itself in Fig. 10. This mode (corresponding to U_{12} and U_{13}) represents an oblique HTW that moves in the $-y$ direction. It is very asymmetric with respect to the lateral midplane. The temporal dynamics of this mode can be seen in the supplementary video 'video_S5', which shows $\hat{\mathbf{U}}_{12} + \hat{\mathbf{U}}_{13}$. Finally, the third mode (corresponding to U_{15} and U_{18}) again represents approximately longitudinal motion at the same frequency of $f \simeq 0.199\,\text{Hz}$ that was measured for $\Delta T = 20\,\text{K}$.

For $\Delta T = 40\,\text{K}$, the primary oscillatory mode (corresponding to U_5 and U_7) has features similar to the case of $\Delta T = 30\,\text{K}$ except for a slightly higher frequency of $f \simeq 0.261\,\text{Hz}$ and the lateral midplane reflection symmetry, which is restored. The second strongest oscillatory mode (corresponding to U_{13} and U_{15}) also shares these same features and is symmetric, but with a dominant frequency of $f \simeq 0.288\,\text{Hz}$. In addition, the larger thermal forcing excites a higher-frequency mode with $f \simeq 0.585\,\text{Hz}$ that appears at relatively low order (U_{22} and U_{24}) in the SVD series. This mode is the second harmonic in space (x and y directions) and time of the previous mode (U_{13} and U_{15}), indicating the importance of a 1:2 resonant interaction. The longitudinal HTW mode no longer appears at low order ($i \lesssim 32$).

The same analysis applied to the case of $W = 12.5\,\text{mm}$, which corresponds to a transverse aspect ratio of $\Gamma_W = 1.8$, gives the results summarized in Fig. 9(b). The character of the leading-order oscillatory modes is analogous to that described for $\Gamma_W = 0.9, 1.2$. In particular, there are primary oblique HTW modes and secondary HTW modes at a slightly lower frequency that correspond, on average, to longitudinal motion. As with $\Gamma_W = 1.2$, the longitudinal HTW mode no longer appears (at low order) for $\Delta T = 40\,\text{K}$ but there is a prominent second harmonic (1:2 resonance). One notable difference from the previous two aspect ratios is the absence of frequency splitting in the oblique HTW modes. As before, their frequency increases with the applied thermal forcing ΔT. With this aspect ratio, the oscillatory thermocapillary flow is symmetric for $\Delta T = 20, 30\,\text{K}$ and slightly asymmetric for $\Delta T = 40\,\text{K}$.

3.3. $W = 6.25\,mm$ ($\Gamma_W = 3.6$)

The case of oscillatory flow in narrow containers with $W = 6.25\,\text{mm}$ ($\Gamma_W = 3.6$) is considered separately in this section due to its more substantial differences with respect to wider domains.

Fig. 11 shows the three lowest-order (distinct) oscillatory modes for $\Delta T = 20\,\text{K}$. The strongest mode U_7, shown in panel (a), is characterized by $(\lambda_x, \lambda_y, \lambda_z) \sim (L/4, 2\,W, 2H)$ and dimensionless wavenumbers $(K_x, K_y, K_z) \sim (4, 0.5, 0.5)$. The spectrogram reveals a single dominant frequency $f \simeq 0.195\,\text{Hz}$. Note that this oscillatory mode (and its phase-shifted partner U_9) is now associated with a longitudinal HTW.

The second strongest distinct oscillatory mode U_{23}, shown in panel (b), corresponds to a HTW with $(K_x, K_y, K_z) \sim (4, 1, 0.5)$ that is antisymmetric with respect to the lateral midplane. It is notable that this mode (and its phase-shifted partner U_{30}) appears only during a relatively short stage of the melting process. Consequently, the dynamics of thermocapillary-driven melting are largely symmetric in this case except for the period between $t \approx 400\,\text{s}$ and $800\,\text{s}$ when this antisymmetric HTW mode appears.

The third strongest mode, represented in panel (c) by U_{32}, is a second harmonic of the primary mode, with a frequency and longitudinal wavenumber that are double those of the mode in panel (a). Recall that this type of 1:2 spatiotemporal resonance was also observed for HTWs with $\Gamma_W = 1.2$ and 1.8.

The temporal dynamics of the two most prominent HTW modes can be seen in the supplementary video 'video_S6', which shows $\hat{\mathbf{U}}_7 + \hat{\mathbf{U}}_9$ and $\hat{\mathbf{U}}_{23} + \hat{\mathbf{U}}_{30}$ (the transient asymmetric mode).

These results, together with those for increasing thermal forcing $\Delta T = 30, 40\,\text{K}$ are summarized in Fig. 12, which shows that, as with other aspect ratios, the frequency of oscillatory flow tends to increase with ΔT. The flow is generally asymmetric with respect to reflection in y and the strongest oscillatory mode is similar to the second strongest mode (i.e., the antisymmetric one) observed for $\Delta T = 20\,\text{K}$. The second

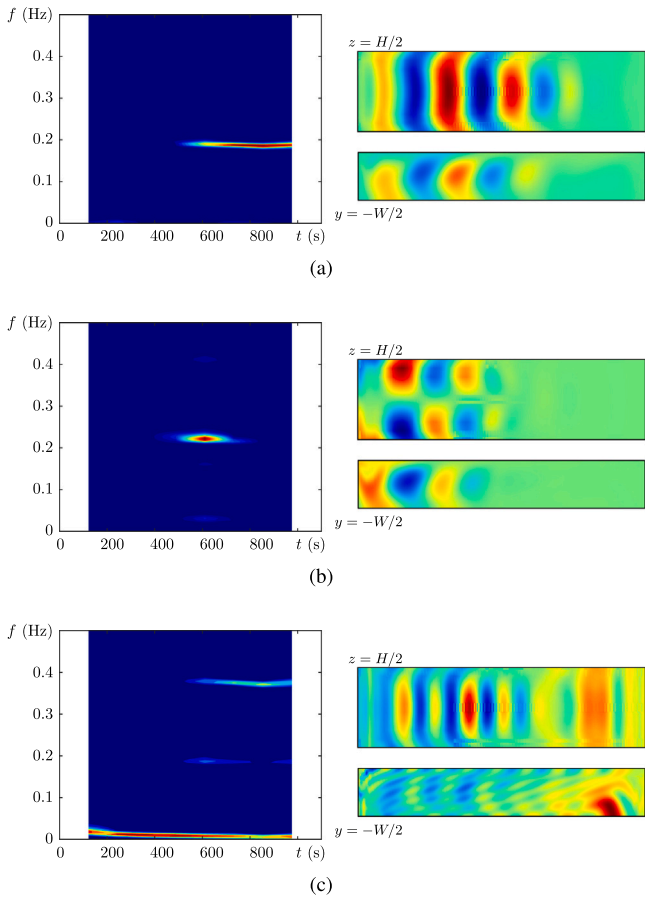

Fig. 11. Principal oscillatory modes for $W = 6.25\,\text{mm}$ ($\Gamma_W = 3.6$) and $\Delta T = 20\,\text{K}$: (a) U_7, (b) U_{23}, (c) U_{32}. The temporal dynamics of the first two modes can be seen in supplementary video 'video_S6', which shows $\hat{\mathbf{U}}_7 + \hat{\mathbf{U}}_9$ and $\hat{\mathbf{U}}_{23} + \hat{\mathbf{U}}_{30}$.

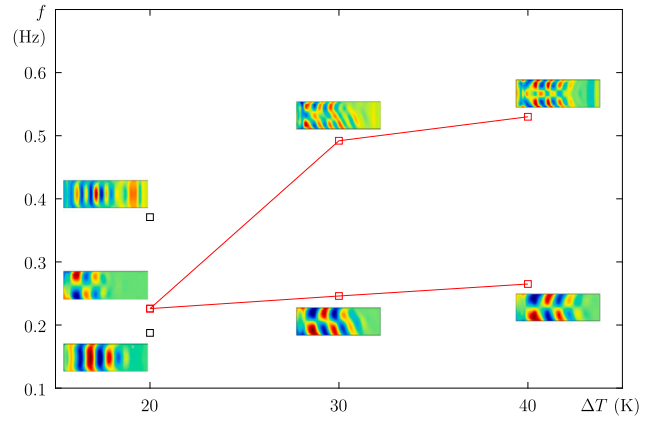

Fig. 12. Diagram summarizing the principal oscillatory modes for $W = 6.25\,\text{mm}$ ($\Gamma_W = 3.6$). The panel shows the dominant frequencies and spatial structures versus the applied thermal forcing ΔT.

harmonic of this mode also appears at low order in the SVD series. For $\Delta T = 30\,\text{K}$, these two modes have characteristic frequencies $f \simeq 0.246$ and $0.492\,\text{Hz}$, respectively, which confirms their resonant character. Longitudinal HTWs no longer appear at low order for $\Delta T = 30,\ 40\,\text{K}$.

Fig. 13 shows the three strongest oscillatory modes for $\Delta T = 40\,\text{K}$ in more detail. The primary mode U_5, shown in panel (a), is characterized by the dimensionless wavenumbers $(K_x,\ K_y,\ K_z) \sim (3.5,\ 0.75,\ 0.5)$ and a

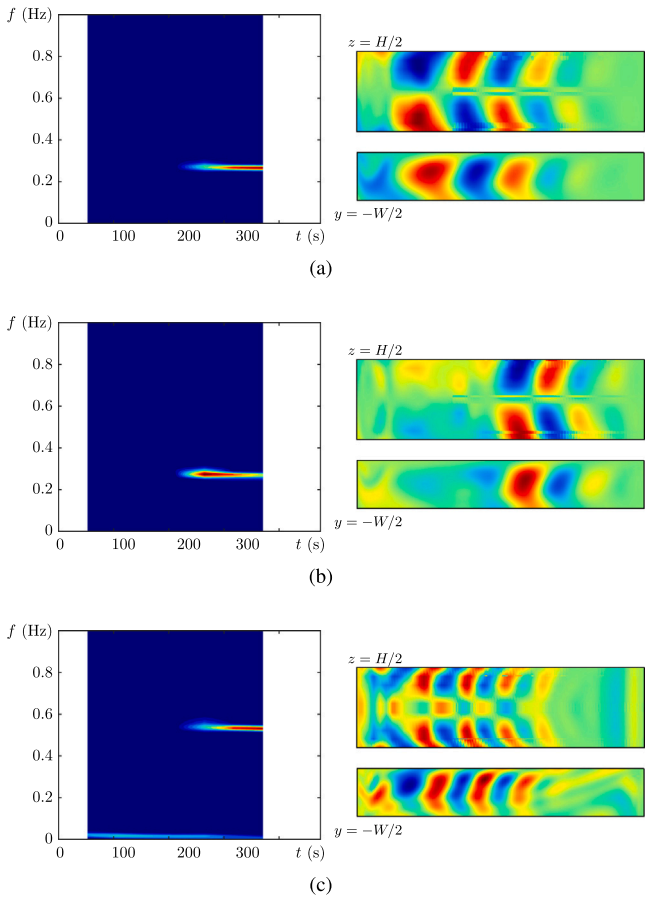

Fig. 13. Principal oscillatory modes for $W = 6.25\,\text{mm}$ ($\Gamma_W = 3.6$) and $\Delta T = 40\,\text{K}$: (a) U_5, (b) U_{16}, (c) U_{20}. The temporal dynamics of the first two modes can be seen in supplementary video 'video_S7', which shows $\hat{\mathbf{U}}_5 + \hat{\mathbf{U}}_8$ and $\hat{\mathbf{U}}_{16} + \hat{\mathbf{U}}_{18}$.

frequency $f = 0.265\,\text{Hz}$ (as is its phase-shifted partner U_8). It is antisymmetric with respect to midplane refection. The second strongest distinct mode U_{16}, shown in panel (b), shares the same dominant wavenumbers and frequency and is also antisymmetric (as is its phase-shifted partner U_{18}). It differs in its spatial profile, which is more concentrated toward the second half of the domain (near the cold wall or melting front). Recall that this type of behavior was mentioned earlier: sometimes, the same HTW is represented by groups of modes, with singular values of different magnitude, corresponding to distinct stages of the melting process. The supplementary video 'video_S7' illustrates this by showing the temporal evolution of $\hat{\mathbf{U}}_5 + \hat{\mathbf{U}}_8$ and $\hat{\mathbf{U}}_{16} + \hat{\mathbf{U}}_{18}$.

Finally, the third strongest mode U_{20} (its phase-shifted partner being U_{22}) is shown in panel (c). This mode is a second harmonic of the first two modes, with $f \simeq 0.531\,\text{Hz}$, and $(K_x,\ K_y,\ K_z) \sim (7,\ 1.5,\ 0.5)$. It is symmetric under a midplane reflection.

3.4. Summary of results

An overview of the results obtained for the different widths and applied temperatures is provided in Fig. 14.

For each spanwise aspect ratio considered, both oblique and (approximately) longitudinal HTWs are seen to dominate the dynamics of oscillatory thermocapillary-driven PCM melting. For $\Delta T = 20\,\text{K}$, both of these modes are symmetric with respect to lateral midplane reflection and unique (at least, at low order) except for the narrowest container with $W = 6.25\,\text{mm}$. In that case, the oblique HTW does not appear at low order but there is a prominent second harmonic of the main

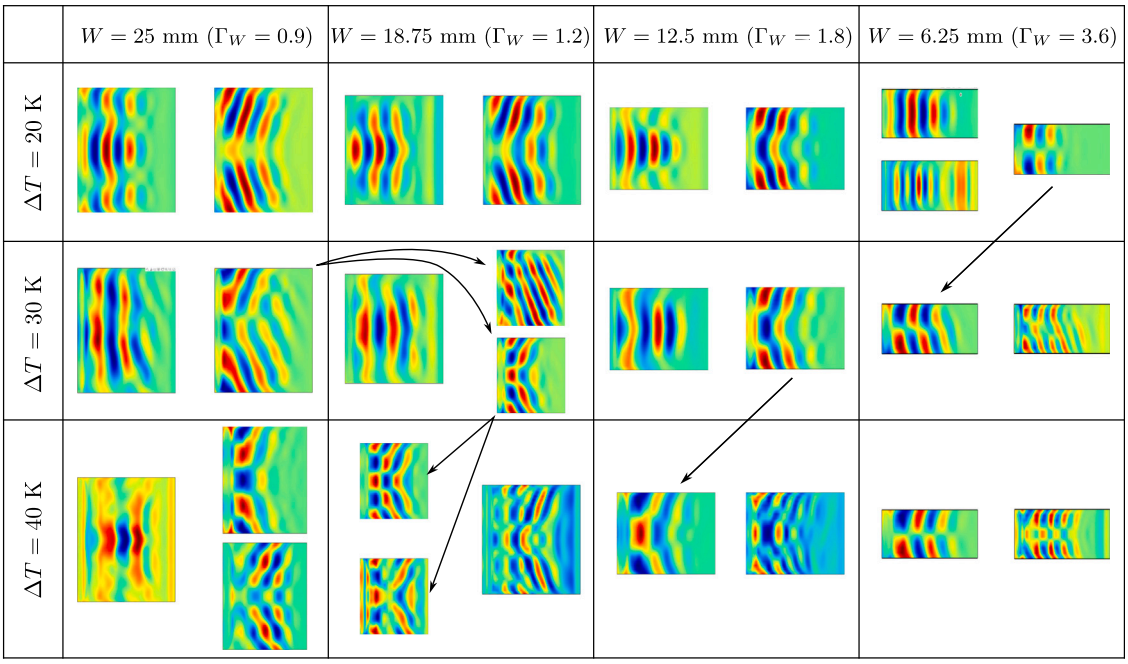

Fig. 14. Summary of the dominant oscillatory modes and their spatial structure for all combinations of $\Delta T = 20, 30, 40$ K and $W = 25, 18.75, 12.5, 6.25$ mm. Arrows indicate the continuity (similarity) of modes as well as splitting.

longitudinal mode and an important asymmetric mode that appears temporarily between approximately 400 and 800 s.

For $\Delta T = 30$ K, both the oblique and longitudinal HTW modes are asymmetric when $W = 25, 18.75$ mm. Furthermore, the oblique mode splits into two for the latter width, with one representing an asymmetric oblique wave that travels almost purely in the $-y$ (or $+y$) direction. This (low-order) splitting and asymmetry disappear when the width is decreased to $W = 12.5$ mm. In the narrowest container with $W = 6.25$ mm, the longitudinal mode no longer appears at low order but there is an oblique mode and its second harmonic, both of which are asymmetric.

For $\Delta T = 40$ K, the longitudinal HTW mode is only observed (at low order) when $W = 25$ mm. For this width, as well as $W = 18.75$ mm, the oscillatory dynamics are symmetric but they are asymmetric for $W = 12.5$ mm (albeit only slightly so) and for $W = 6.25$ mm. Splitting of the oblique HTW is observed with $W = 18.75$ mm while a prominent 1:2 spatiotemporal resonance is seen for this spanwise aspect ratio as well as the two narrower containers.

4. Conclusions

PCMs are important for temperature control, but organic PCMs, in particular, have low thermal conductivity that reduces their responsiveness. Convective flows can improve heat transfer, and when the buoyancy force is absent, as in microgravity applications, thermocapillary convection is the natural alternative. With this motivation, the MarPCM experiment will investigate the thermocapillary-driven melting of PCMs in microgravity. Previous numerical studies explored the melting process using 2D and 3D models and revealed that while the 2D approximation is relatively accurate for predicting melting rates, 3D effects can be relevant for pattern selection and for dynamics in the oscillatory regime [44].

Here we extended the results of Seta et al. [44] by investigating the effect of lateral width. The melting process was analyzed in cuboidal containers of length $L = 22.5$ mm, height $H = 1.875$ mm, and widths $W = 25, 18.75, 12.5, 6.25$ mm. Due the cost of 3D simulations, only three applied temperature differences were considered for each domain: $\Delta T = 20, 30, 40$ K.

The simulation results were analyzed with POD, implemented via SVD, which was seen to provide a convenient way to analyze and interpret the dynamics of the melting process. The first several leading-order modes describe quasi-steady dynamics associated with the slow progression of the solid/liquid front and the evolving liquid domain. The loss of stability to oscillatory flow is captured by modes at (slightly) higher order. For each spanwise aspect ratio considered, the oscillatory dynamics is characterized by the appearance of oblique and longitudinal hydrothermal traveling waves (HTWs) — typically represented by pairs of POD modes that are shifted in phase. The properties of these modes, including approximate spatial wavenumbers and dominant frequencies, depends on ΔT.

For $\Delta T = 20$ K, these modes are symmetric with respect to the lateral midplane of the container, except when $W = 6.25$ mm, where the oblique HTW is absent at low order. Instead, a prominent second harmonic of the primary longitudinal mode appears, along with a transient asymmetric mode. At $\Delta T = 30$ K, both the oblique and longitudinal HTW modes are asymmetric for $W = 25$ mm and 18.75 mm. Furthermore, for $W = 18.75$ mm, the oblique mode splits into two, though this splitting, as well as the asymmetry, disappears if the width is reduced further to $W = 12.5$ mm. In the narrowest container with $W = 6.25$ mm, the longitudinal mode is absent at low order and the oscillatory flow is dominated by an asymmetric oblique mode and its second harmonic. At $\Delta T = 40$ K, the longitudinal HTW mode is present at low order only when $W = 25$ mm. For this width and for $W = 18.75$ mm, the oscillatory flow is symmetric, whereas for $W = 12.5$ and 6.25 mm, it is asymmetric. A splitting of the oblique HTW occurs for $W = 18.75$ mm, while a prominent 1:2 spatiotemporal resonance is observed for this width and the two smaller ones.

In general, the results presented here illustrate the complex, three-dimensional character of the oscillatory dynamics that can arise in cuboidal containers with melting PCMs. While the specific modes that appear are sensitive to aspect ratio and Marangoni number, it is not surprising to observe oblique hydrothermal traveling waves, which are known to onset first in extended liquid systems with thermocapillary flow, or longitudinal ones, which may have a slightly higher critical Marangoni number in that (extended, liquid) system [33] but are presumably less affected by the constraints of the lateral boundary

conditions in the system treated here. The 1:2 spatiotemporal resonance is also a well known feature of numerous pattern selection problems.

Several topics suggest themselves for further investigation. First, it may be of interest to determine the critical ΔT associated with the onset of oscillatory flow in each geometry. Since POD was seen to be an efficient method for locating oscillatory modes and extracting their main features, it could also be used to estimate onset by looking at the extent to which these modes persist during melting and calculating the associated *mode contribution* [35]. Another extension would be the analysis of 3D flows in deeper containers, including the variation in both longitudinal and spanwise aspect ratios. This analysis, covering the transition between shallow and deep containers, will be carried out elsewhere. From an experimental perspective, the present methodology could be used to determine the most sensitive regions of the PCM domain, as proposed by the Discrete Empirical Interpolation Method [68,69]. This would help define the optimal placement for a finite set of thermocouples whose measurements can be used to reconstruct the temperature field across the entire PCM.

CRediT authorship contribution statement

P. Salgado Sánchez: Investigation, Writing – original draft, Formal analysis, Conceptualization. **X. Ruiz:** Writing – original draft, Software, Data curation. **J. Massons:** Investigation, Writing – original draft, Software. **J. Porter:** Conceptualization, Formal analysis, Writing – original draft, Supervision. **J.M. Ezquerro:** Formal analysis, Supervision, Writing – original draft. **Jna. Gavaldà:** Software, Writing – original draft, Conceptualization.

Declaration of competing interest

The authors report no conflict of interest.

Acknowledgments

The work of P.S.S, J.P. and J.M.E. was supported by the Ministerio de Ciencia e Innovación, Spain (y Universidades) under Project Nos. PID2020-115086GB-C31 and PID2023-149539NB-C31, and by the Spanish User Support and Operations Centre (E-USOC), Center for Computational Simulation (CCS). The work of X.R., J.M. and Jna.G. was also supported by the Ministerio de Ciencia Ciencia e Innovación, Spain (y Universidades) under Project Nos. PID2023-149539NB-C32 and PCI2024-155034-02.

Appendix A. Supplementary data

Supplementary material related to this article can be found online at https://doi.org/10.1016/j.icheatmasstransfer.2025.109289.

Data availability

No data was used for the research described in the article.

References

[1] R. Kandasamy, X.-Q. Wang, A.S. Mujumdar, Application of phase change materials in thermal management of electronics, Appl. Therm. Eng. 27 (2007) 2822–2832.
[2] N. Chaiyat, T. Kiatsiriroat, Energy reduction of building air-conditioner with phase change material in thailand, Case Stud. Therm. Eng. 4 (2014) 175–186.
[3] K.O. Lee, M.A. Medina, Using phase change materials for residential air conditioning peak demand reduction and energy conservation in coastal and transitional climates in the state of california, Energy Build. 116 (2016) 69–77.
[4] P.H. Biwole, P. Eclache, F. Kuznik, Phase change materials to improve solar panel's performace, Energy Build. 62 (2013) 59–67.
[5] C.J. Ho, B.-T. Jou, C.-M. Lai, C.-Y. Huang, Performance assessment of a BIPV integrated with a layer of water-saturated MEPCM, Energy Build. 67 (2013) 322–333.
[6] J. Hirschey, K.R. Gluesenkamp, A. Mallow, S. Graham, Review of inorganic salt hydrates with phase change temperature in range of 5°c to 60 °c and material cost comparison with common waxes, in: Proceedings of 5th International High Performance Buildings Conference At Purdue, July 9-12, 2018, pp. 1–10.
[7] F. Agyenim, P. Eames, M. Smyth, A comparison of heat transfer enhancement in a medium temperature thermal energy storage heat exchanger using fins, Sol. Energy 83 (2009) 1509–1520.
[8] M. Medrano, M. Yilmaz, M. Nogués, I. Martorell, J. Roca, L.F. Cabeza, Experimental evaluation of commercial heat exchangers for use as pcm thermal storage systems, Appl. Energy 86 (2009) 2047–2055.
[9] R. Koželj, E. Osterman, F. Leonforte, C. Del Pero, A. Miglioli, E. Zavrl, R. Stropnik, N. Aste, U. Stritih, Phase-change materials in hydronic heating and cooling systems: A literature review, Materials 13 (2020).
[10] N.S. Dhaidan, J.M. Khodadadi, T.A. Al-Hattab, S.M. Al-Mashat, Experimental and numerical investigation of melting of NePCM inside an annular container under a constant heat flux including the effect of eccentricity, Int. J. Heat Mass Transfer 67 (2013) 455–468.
[11] S. Madruga, C. Mendoza, Heat transfer performance and thermal energy storage in nano-enhanced phase change materials driven by thermocapillarity, Int. Commun. Heat Mass Transfer 129 (2021) 105672.
[12] P. Salgado Sanchez, J.M. Ezquerro, J. Porter, J. Fernandez, J. Rodriguez, I. Tinao, V. Lapuerta, A. Laveron-Simavilla, X. Ruiz, F. Gavalda, M.M. Mounir Bou-Ali, J. Ortiz, The effect of thermocapillary convection on pcm melting in microgravity: results and expectations, in: Proceeding of the 72th International Astronautical Conference, IAC, 2020.
[13] C. Gau, R. Viskanta, Melting and solidification of a pure metal on a vertical wall, Trans. ASME 108 (1986) 174–181.
[14] S.K. Roy, S. Sengupta, Gravity-assisted melting in a spherical enclosure: effects of natural convection, Int. J. Heat Mass Transfer 33 (1990) 1135–1147.
[15] Y. Wang, A. Amiri, K. Vafai, An experimental investigation of the melting process in a rectangular enclosure, Int. J. Heat Mass Transfer 42 (1999) 3659–3672.
[16] J.M. Khodadadi, Y. Zhang, Effects of buoyancy-driven convection on melting within spherical containers, Int. J. Heat Mass Transfer 44 (2001) 1605–1618.
[17] N.S. Dhaidan, J.M. Khodadadi, Melting and convection of phase change materials in different shape containers: A review, Renew. Sustain. Energy Rev. 43 (2015) 449–477.
[18] R. Varas, U. Martinez, K. Olfe, P. Salgado Sánchez, J. Porter, J.M. Ezquerro, Effects of thermocapillary and natural convection during the melting of phase change materials with a liquid bridge geometry, Microgravity Sci. Technol. 35 (2023) 17.
[19] B.M. Diaconu, M. Cruceru, L. Anghelescu, Phase change materials in space systems. fundamental applications, materials and special requirements - a review, Acta Astronaut. 216 (2023) 163–213.
[20] R. Creel, Apollo rover lessons learned: Applying thermal control experiences on apollo lunar rover project to rovers for future space exploration, 2007.
[21] A. Borshchak Kachalov, P. Salgado Sanchez, U. Martinez, J.M. Ezquerro, Preliminary design of a space habitat thermally controlled using phase change materials, Thermo 3 (2023) 232–247.
[22] C. Ongil, U. Martinez, P. Salgado Sanchez, A. Borshchak Kachalov, J.M. Ezquerro, K. Olfe, Laboratory experiments on passive thermal control of space habitats using phase-change materials, Thermo 4 (2024) 461–474.
[23] A. Borshchak Kachalov, P. Salgado Sanchez, M.T. Mollah, J.M. Ezquerro, J. Spangenberg, B. Seta, Numerical analysis of coaxially 3d printed lunar habitats: integrating regolith and pcm for passive temperature control, Microgravity Science and Technology 37 (2025) 38.
[24] J.M. Ezquerro, P. Salgado Sanchez, A. Bello, J. Rodriguez, V. Lapuerta, A. Laveron-Simavilla, Experimental evidence of thermocapillarity in phase change materials in microgravity: measuring the effect of marangoni convection in solid/liquid phase transitions, Int. Commun. Heat Mass Transfer 113 (2020) 104529.
[25] P. Salgado Sanchez, J.M. Ezquerro, J. Porter, J. Fernandez, I. Tinao, Effect of thermocapillary convection on the melting of phase change materials in microgravity: experiments and simulations, Int. J. Heat Mass Transfer 154 (2020a) 119717.
[26] P. Salgado Sanchez, J.M. Ezquerro, J. Fernandez, J. Rodriguez, Thermocapillary effects during the melting of phase change materials in microgravity: heat transport enhancement, Int. J. Heat Mass Transfer 163 (2020b) 120478.
[27] R. Varas, P. Salgado Sanchez, J. Porter, J.M. Ezquerro, V. Lapuerta, Thermocapillary effects during the melting in microgravity of phase change materials with a liquid bridge geometry, Int. J. Heat Mass Transfer 178 (2021) 121586.
[28] A. Borshchak Kachalov, P. Salgado Sánchez, U. Martínez, J. Fernández, J.M. Ezquerro, Optimization of thermocapillary-driven melting in trapezoidal and triangular geometry in microgravity, Int. J. Heat Mass Transfer 185 (2022) 122427.
[29] R. Garcia-Roco, P. Salgado Sanchez, A. Bello, K. Olfe, J. Rodriguez, Dynamics of pcm melting driven by a constant heat flux at the free surface in microgravity, Therm. Sci. Eng. Prog. 48 (2024) 102378.
[30] V. Shevtsova, A. Nepomnyashchy, J.C. Legros, Thermocapillary-buoyancy convection in a shallow cavity heated from the side, Phys. Rev. E 67 (2003) 066308.

[31] A.K. Sen, S.H. Davis, Steady thermocapillary flows in two-dimensional slots, J. Fluid Mech. 121 (1982) 163–186.
[32] D. Schwabe, A. Scharmann, Some evidence for the existence and magnitude of a critical marangoni number of the onset of oscillatory flow in crystal growth melts, J. Cryst. Growth 46 (1979) 125–131.
[33] M.K. Smith, S.H. Davis, Instabilities of dynamic thermocapillary liquid layers. part 1. Convective instabilities, J. Fluid Mech. 132 (1983) 119–144.
[34] M.K. Smith, Instability mechanisms in dynamic thermocapillary liquid layers, Phys. Fluids 29 (1986) 3182.
[35] P. Salgado Sanchez, J.M. Ezquerro, J. Fernandez, J. Rodriguez, Thermocapillary effects during the melting of phase change materials in microgravity: steady and oscillatory flow regimes, J. Fluid Mech. 908 (2021) A20.
[36] P. Salgado Sanchez, J. Porter, J.M. Ezquerro, I. Tinao, A. Laveron-Simavilla, Pattern selection for thermocapillary flow in rectangular containers in microgravity, Phys. Rev. Fluids 7 (2022) 053502.
[37] N. Martínez, P. Salgado Sanchez, J. Porter, J.M. Ezquerro, Effect of surface heat exchange on phase change materials melting with thermocapillary flow in microgravity, Phys. Fluids 33 (2021) 083611.
[38] N. Martinez Figueira, P. Salgado Sanchez, A. Bello, K. Olfe, J. Rodriguez, Effect of surface heat exchange on phase change materials melting with thermocapillary flow in microgravity, Phys. Fluids 35 (2023) 084115.
[39] P. Salgado Sánchez, J.M. Ezquerro, D. Gligor, U. Martinez, J. Fernandez, I. Tinao, The effect of marangoni convection on heat transfer in phase change materials experiment, from a student project to the international space station, in: Proccedings of the 4th Symposium on Space Education Activities, 2022, pp. 1–6.
[40] J. Porter, A. Laverón-Simavilla, M. Bou-Ali, X. Ruiz, F. Gavalda, J. Ezquerro, P. Salgado Sánchez, U. Martínez, D. Gligor, I. Tinao, J. Gómez, J. Fernández, J. Rodríguez, A.B. Kachalov, V. Lapuerta, B. Šeta, J. Massons, D. Dubert, A. Sanjuan, V. Shevtsova, L. García-Fernández, The "effect of marangoni convection on heat transfer in phase change materials" experiment, Acta Astonautica 210 (2023) 212–223.
[41] U. Martínez, J. Ezquerro, J. Fernandez, K. Olfe, The effect of Marangoni convection on heat transfer in phase change materials experiment: Design and performance of the cuboidal cell, Acta Astronaut. 216 (2024) 152–162.
[42] B. Seta, D. Dubert, J. Massons, J. Gavalda, M.M. Bou-Ali, X. Ruiz, Effect of marangoni induced instabilities on a melting bridge under microgravity conditions, Int. J. Heat Mass Transfer 179 (2021) 121665.
[43] J.M. Ezquerro, A. Bello, P. Salgado Sanchez, A. Laveron-Simavilla, V. Lapuerta, The thermocapillary effects in phase change materials in microgravity experiment: design, preparation and execution of a parabolic flight experiment, Acta Astronaut. 162 (2019) 185–196.
[44] B. Seta, P. Salgado Sanchez, D. Dubert, J. Massons, J. Gavalda, J. Porter, M. Mounir Bou-Ali, X. Ruiz, V. Shevtsova, Three-dimensional effects during thermocapillary-driven melting of pcms in cuboidal containers in microgravity, Int. Commun. Heat Mass Transfer 150 (2024) 107198.
[45] G. Golub, C.V. Loan, Matrix Computation, second ed. Johns Hopkins University Press, 2013.
[46] I. Markovsky, S.V. Huffel, Overview of total least squares methods, Signal Process. 87 (2007) 2283–2302.
[47] V. Muralidharan, K.C. Howell, Leveraging stretching directions for stationkeeping in earth-moon halo orbits, Adv. Space Res. 69 (2022) 620–646.
[48] I. Mademlis, A. Tefas, I. Pitas, Regularized svd-based video frame saliency for unsupervised activity video summarization, in: Proceesing of the 2018 IEEE International Conference on Acoustics, Speech and Signal Processing, ICASSP, 2018, pp. 2691–2695.
[49] P. Salgado Sánchez, F. Varas, J. Porter, D. Gligor, Optical processing of melting pcm bridges in microgravity using SVD and ANNs, Microgravity Sci. Technol. 37 (2025a) 12.
[50] P. Salgado Sánchez, F. Varas, J. Porter, C. Haukes, SVD-AMM-based processing of melting pcm bridges experiments in microgravity: sensitivity to image defects and data repairing algorithms, Microgravity Sci. Technol. (2025b) (accepted).
[51] S. Walton, O. Hassan, K. Morgan, Reduced order modelling for unsteady fluid flow using proper orthogonal decomposition and radial basis functions, Appl. Math. Model. 37 (2013) 8930–8945.
[52] E.M. Alawadhi, Thermal analysis of a building brick containing phase change material, Energy Build. 40 (2008) 351–357.
[53] D.R. Lide, Handbook of chemistry and physics, 2014.
[54] V.R. Voller, M. Cross, N.C. Markatos, An enthalpy method for convection/diffusion phase change, Internat. J. Numer. Methods Engrg. 24 (1987) 271–284.
[55] V. Voller, C. Prakash, A fixed grid numerical modelling methodology for convection–diffusion mushy region phase-change problems, Int. J. Heat Mass Transfer 30 (1987) 1709–1719.
[56] C.R. Swaminathan, V.R. Voller, On the enthalpy method, international, J. Numer. Methods Heat Fluid Flow 3 (1993) 233–244.
[57] B. Šeta, P.S. Sánchez, J. Massons, J. Gavaldá, J. Porter, M. Bou-Ali, X. Ruiz, V. Shevtsova, Three-dimensional effects during the melting of phase-change materials with thermocapillary flow in microgravity, in: 27th European Low Gravity Research Association Biennial Symposium, Lisbon, 2022.
[58] C. Velez, M. Khayet, J.M. Ortiz, Temperature-dependent thermal properties of solid/liquid phase change even-numbered n-alkanes: n-hexadecane, n-octadecane and n-eicosane, Appl. Energy 143 (2015) 383–394.
[59] S. Madruga, C. Mendoza, Enhancement of heat transfer rate on phase change materials with thermocapillary flows, Eur. Phys. J. Spec. Top. 226 (2017) 1169–1176.
[60] B. Seta, D. Dubert, M. Prats, J. Gavalda, J. Massons, M. Bou-Ali, X. Ruiz, V. Shevtsova, Transitions between nonlinear regimes in melting and liquid bridges in microgravity, Int. J. Heat Mass Transfer 193 (2022) 122984.
[61] J.M. Montanero, C. Ferrero, V.M. Shevtsova, Experimental study of the free surface deformation due to thermal convection in liquid bridges, Exp. Fluids 45 (2008) 1087–1101.
[62] V. Voller, A. Brent, C. Prakash, The modelling of heat, mass and solute transport in solidification systems, Int. J. Heat Mass Transfer 32 (1989) 1719–1731.
[63] F.P. Kärrholm, Rhie-chow interpolation in openfoam, 2007.
[64] S. Madruga, G.S. Mischlich, Melting dynamics of a phase change material (PCM) with dispersed metallic nanoparticles using transport coefficients from empirical and mean field models, Appl. Therm. Eng. 124 (2017) 1123–1133.
[65] V. Dolean, P. Jolivet, F. Nataf, An Introduction To Domain Decomposition Methods: Algorithms, Theory and Parallel Implementation, Technical Report, 2015.
[66] C. Eckart, G. Young, The approximation of one matrix by another of lower rank, Psychometrika 1 (1936) 211–218.
[67] L. Mirsky, Symmetric gauge functions and unitarily invariant norms, Q. J. Math. 11 (1936) 50–59.
[68] S. Chaturantabut, D.C. Sorensen, Discrete empirical interpolation for nonlinear model reduction, in: Proceedings of the 48h IEEE Conference on Decision and Control (CDC) Held Jointly with 2009 28th Chinese Control Conference, 2009, pp. 4316–4321.
[69] E.P. Hendryx Lyons, The discrete empirical interpolation method in class identification and data summarization, WIREs Comput. Stat. 16 (2024) e1653.